Chemical Science

ROYAL SOCIETY OF CHEMISTRY

EDGE ARTICLE

View Article Online
View Journal | View Issue

Cite this: *Chem. Sci.*, 2025, **16**, 19806

All publication charges for this article have been paid for by the Royal Society of Chemistry

Photoresponsive luminescent single-molecule magnets based on dysprosium–anthracene complexes: regulating the de-dimerization temperature of the photocycloaddition product by co-ligand

Ye-Hui Qin,†[a] Xiu-Fang Ma,†[a] Xinlan Hou,†[b] Xin-Da Huang,[a] Song-Song Bao,[a] Yuxi Tian,[b] Yi-Quan Zhang *[c] and Li-Min Zheng *[a]

Lanthanide–anthracene complexes that can undergo reversible photocycloaddition reaction are attractive for the development of photoresponsive luminescent single-molecule magnets (SMMs). However, how to regulate the de-dimerization temperature of *in situ* formed dianthracenes remains an open question. Here, we report two binuclear dysprosium–anthracene complexes $[Dy_2(SCN)_4(L)_2(depma)_2(DEPP)_2]$ (**1**) and $[Dy_2(SCN)_4(L^{Me})_2(depma)_2(DEPP)_2]$ (**2**), where L is 2,6-dimethoxyphenol, L^{Me} is 4-methyl-2,6-dimethoxyphenol, depma is 9-diethyl-phosphonomethylanthracene, and DEPP is diethylpropylphosphonate. Both undergo single-crystal-to-single-crystal (SC–SC) photocycloaddition reactions to form the 1D coordination polymers $[Dy_2(SCN)_4L_2(depma_2)(DEPP)_2]_n$ (**1UV**) and $[Dy_2(SCN)_4(L^{Me})_2(depma_2)(DEPP)_2]_n$ (**2UV**), where $depma_2$ is photo-dimerized depma, concomitant with changes in photoluminescence and magnetic properties. Interestingly, the de-dimerization temperatures of **1UV** (80 °C) and **2UV** (71 °C) are much lower than those of the known lanthanide–dianthracene complexes (≥100 °C). We found that the stability of *in situ* formed dianthracene depends largely on the spacing and slip angle of the anthracene pair in the original complex, with spacing being more important, and these parameters can be modulated by choosing suitable co-ligands. In addition, we investigated the kinetics of the photocycloaddition reaction of **1** at different temperatures and found that the rate of the reaction reached a maximum at the temperature of complete de-dimerization.

Received 9th June 2025
Accepted 14th September 2025

DOI: 10.1039/d5sc04192a

rsc.li/chemical-science

Introduction

Lanthanide-based single-molecule magnets (Ln-SMMs) have attracted considerable attention for their potential applications in information storage, molecular devices, and sensors.[1–5] Photo-responsive Ln-SMMs are of particular interest because their magnetic and optical properties can be manipulated by light,[6–8] akin to the other emissive magnetic systems such as spin crossover and metal–cyanide compounds.[9] Previous studies have demonstrated that the incorporation of photo-active components is an effective method for realizing photoresponsive Ln-SMMs with tunable magnetic and optical properties,[10–15] but reports showing synergistic modulation of luminescence and SMM properties are still limited.[16,17] Among the known photoactive components, anthracene and its derivatives are well recognized for their rich photophysical properties and the ability to undergo [4 + 4] photocycloaddition reaction under UV light irradiation.[18–22] Over the past few years, we and others have constructed a series of lanthanide–anthracene complexes that exhibit light-triggered significant changes in luminescence and SMM properties.[23–26] This change is caused by the structural transformation induced by photocycloaddition of the face-to-face π–π interacting anthracene pairs. More interestingly, the process is reversible, with complete recovery to the initial un-dimerized state upon heating for a few minutes.[23,25] The temperature at which the *in situ* formed di-anthracene undergoes de-dimerization is about 100 °C or more. This fact raises the question: can we regulate the de-dimerization temperature of *in situ* formed Ln-dianthracene complexes to lower temperatures for practical applications?

Our previous work has shown that the Ln-dianthracene compounds formed using pre-photodimerized dianthracene

[a]*State Key Laboratory of Coordination Chemistry, School of Chemistry and Chemical Engineering, Collaborative Innovation Center of Advanced Microstructures, Nanjing University, Nanjing 210023, P. R. China. E-mail: lmzheng@nju.edu.cn*

[b]*State Key Laboratory of Analytical Chemistry for Life Science, Key Laboratory of Mesoscopic Chemistry of MOE, School of Chemistry and Chemical Engineering, Nanjing University, Nanjing 210023, China*

[c]*Ministry of Education Key Laboratory of NSLSCS, School of Physical Science and Technology, Nanjing Normal University, Nanjing 210023, P. R. China. E-mail: zhangyiquan@njnu.edu.cn*

† These authors contributed equally to this work.

ligands have much higher de-dimerization temperatures (140–190 °C)[27–31] than those formed *in situ* (*ca.* 100–140 °C).[23,25,32,33] This result is reasonable because structural transformation induced by photocycloaddition involves rearrangement of the positions of the metal ions and ligands, which is not trivial in the solid state.[23,25,26] As a consequence, dianthracenes formed by *in situ* solid-state photochemical reactions are usually not in their lowest energy state and are therefore less stable than those formed by pre-photodimerization reaction.[34] We envision that the stability of dianthracene formed *in situ* may be related to the stacking pattern of the anthracene pairs prior to light irradiation. The larger the slip angle and plane-to-plane distance of the two anthracene moieties, the less stable the dianthracene is, and hence the lower the temperature of de-dimerization. Thus, in order to regulate the de-dimerization temperature of lanthanide–anthracene complexes after photocycloaddition, it is necessary to change the stacking pattern of the anthracene moieties, which can be achieved by selecting a suitable auxiliary ligand or through ligand modification.[35,36]

To demonstrate the above concept, we report here two Dy-anthracene complexes, $[Dy_2(SCN)_4(L)_2(depma)_2(DEPP)_2]$ (**1**) and $[Dy_2(SCN)_4(L^{Me})_2(depma)_2(DEPP)_2]$ (**2**), where L is 2,6-dimethoxyphenol, L^{Me} is 4-methyl-2,6-dimethoxyphenol, depma is 9-diethyl-phosphonomethylanthracene, and DEPP is diethylpropylphosphonate $[CH_3CH_2CH_2PO(OCH_2CH_3)_2]$ (Scheme 1). Both can undergo photocycloaddition reaction under UV light irradiation in a single-crystal-to-single-crystal (SC–SC) fashion to form the one-dimensional (1D) coordination polymers $[Dy_2(SCN)_4(L)_2(depma_2)(DEPP)_2]_n$ (**1UV**) and $[Dy_2(SCN)_4(L^{Me})_2(depma_2)(DEPP)_2]_n$ (**2UV**), in which $depma_2$ is the photodimerized depma. Notably, compounds **1** and **2** have very similar binuclear structures except that the bridging 2,6-dimethoxyphenol ligand in **2** has an additional methyl group. Such a small difference leads to distinct changes in the stacking pattern of anthracene pairs. Moreover, the structure of **1** is similar to the known compound $[Dy_2(SCN)_4(L)_2(depma)_2(H_2O)_2]$ (**3**) except for the auxiliary ligand DEPP.[32] Compared to H_2O, DEPP has large alkyl groups which may cause steric hindrance and affect the stacking of anthracene groups. As a result, the slip angle (θ) and plane-to-plane distance (d_{pp}) decrease in the following order: **2** (24.6°, 3.503 Å) > **1** (19.7°, 3.443 Å) > **3** (16.9°, 3.410 Å). Accordingly, the de-dimerization temperature of the photocycloaddition products increases in the sequence: **2UV** (71 °C) < **1UV** (80 °C) < **3UV** (100 °C). As far as we are aware, **2UV** shows the lowest de-dimerization temperature among the known metal–dianthracene complexes. We also studied the kinetics of photocycloaddition reaction of compound **1** at different temperatures and found that the reaction rate reached a maximum at the temperature of complete de-dimerization. This work not only provides a feasible route to regulate the de-dimerization temperature of metal–anthracene complexes after photocycloaddition, but also may shed light on the development of anthracene-based photoresponsive materials for practical applications.

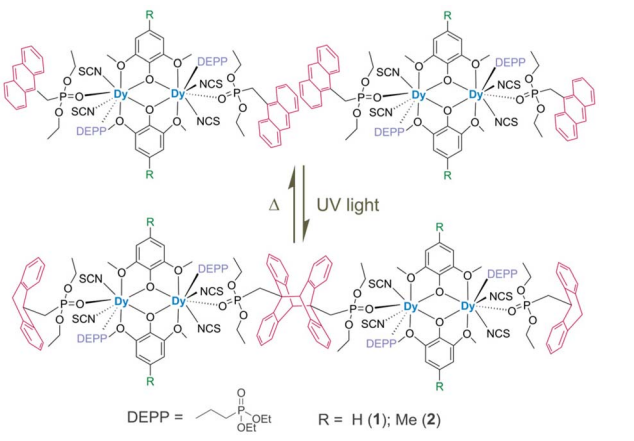

Scheme 1 Structural transformation of an anthracene pair after UV light irradiation.

Results and discussion

Crystal structures

Single-crystal structure analyses revealed that compounds **1** and **2** crystallized in the triclinic $P\bar{1}$ space group (Tables 1 and S1). As shown in Fig. 1a, compound **1** has a centrosymmetric binuclear structure. The asymmetric unit contains one Dy^{III} ion, two SCN^- ions, one DEPP molecule, one depma, and one L ligand. Each Dy^{III} ion is coordinated with four O atoms (O4, O5, O5A, and O6A) from the two L ligands, one O atom (O7) from DEPP, one O atom (O1) from depma and two N atoms (N1, N2) from SCN^- to form an eight-coordinated $[DyO_6N_2]$ configuration. The Dy–O bond lengths are 2.295(3)-2.657(4) Å, and the Dy–N bond lengths are 2.379(4)–2.392(5) Å (Table S2). According to continuous shape measure (CShM) analysis,[37] the geometry of the $[DyO_6N_2]$ polyhedron in **1** is best described as distorted Bi-augmented trigonal prism J50 (CShM = 2.588, C2v, Table S3). The two equivalent Dy centres are bridged by two oxygen atoms O5 and O5A from two tridentate ligands of L^-, forming a binuclear unit of Dy_2O_2 with a Dy1-O5-Dy1A angle of 114.9° and Dy1···Dy1A distance of 3.871 Å. The two depma ligands locate on the two sides of the Dy_2O_2 dimer and each is π–π interacted with the anthracene groups of the adjacent dimer. Thus, an infinite supramolecular chain is constructed through intermolecular π–π interactions of the anthracene groups (d_{C2-C9A} = 3.771 Å, centre-to-centre distance d_{cc} = 3.773 Å, plane-to-plane distance d_{pp} = 3.443 Å) (Fig. 1b). The slip angle of the anthracene pair, defined as the angle between the centroid–centroid line and the vertical line, is 19.7°. The supramolecular chains are further connected by extensive hydrogen bond interactions through C9–H9···S2, C33–H33B···S2 and C25–H25···S1 contacts (Table S4 and Fig. S1a, S2a, S3a), forming a 3D supramolecular network. The shortest intermolecular Dy···Dy distance is 8.566 Å.

Compound **2** has a similar structure to **1** except that the L ligand is replaced by its methyl derivative, L^{Me} (Fig. 1e). This replacement has an effect on the coordination environment of the Dy centre, as evidenced by the changes in bond lengths and angles (Tables 1 and S5). Accordingly, the $[DyO_6N_2]$ polyhedron in **2** deviates more from the biaugmented trigonal prism (CShM = 2.669 *vs.* 2.588 in **1**). Moreover, the Dy1···Dy1A distance over

Table 1 The cell and structural parameters of **1**, **1UV**, **2** and **2UV**

	1	**1UV**	**2**	**2UV**
T (K)	193	193	193	193
Crystal system	Triclinic	Triclinic	Triclinic	Triclinic
Space group	$P\bar{1}$	$P\bar{1}$	$P\bar{1}$	$P1$
a (Å)	11.510(3)	11.584(1)	11.684(5)	11.753(1)
b (Å)	12.095(4)	12.160(1)	11.772(6)	11.913(1)
c (Å)	15.978(8)	15.597(1)	15.675(7)	15.751(1)
α (°)	75.0(1)	76.6(1)	79.6(1)	77.928(1)
β (°)	77.5(1)	78.8(1)	88.7(1)	87.062(1)
γ (°)	74.4(1)	72.2(1)	72.5(1)	73.664(1)
V (Å^3)	2044.0(1)	2016.7(2)	2021.1(2)	2069.5(2)
Dy1-O5, Dy1-O5A/Å	2.295(3), 2.297(3)	2.311(3), 2.290(3)	2.250(5), 2.284(5)	2.285(4), 2.303(4)
Dy1-O1, Dy1-O7/Å	2.319(3), 2.295(4)	2.314(4), 2.289(4)	2.330(5), 2.271(6)	2.344(4), 2.301(5)
Dy1-O4, Dy1-O6A/Å	2.657(4), 2.596(4)	2.643(4), 2.601(4)	2.635(6), 2.555(6)	2.601(4), 2.649(4)
Dy1-N1, Dy1-N2/Å	2.392(5), 2.379(4)	2.388(5), 2.398(5)	2.388(7), 2.360(7)	2.380(6), 2.389(6)
Dy1⋯Dy1A/Å	3.871(1)	3.888(1)	3.833(1)	3.872(1)
Dy1-O5-Dy1A/°	114.9(1)	115.4(2)	115.4(2)	115.1(1)
Slip angle θ/°	19.7	—	24.6	—
d_{cc}/Å	3.773	—	3.868	—
d_{pp}/Å	3.443	—	3.503	—
d_{C2-C9A}/Å	3.771	1.669	3.860	1.689

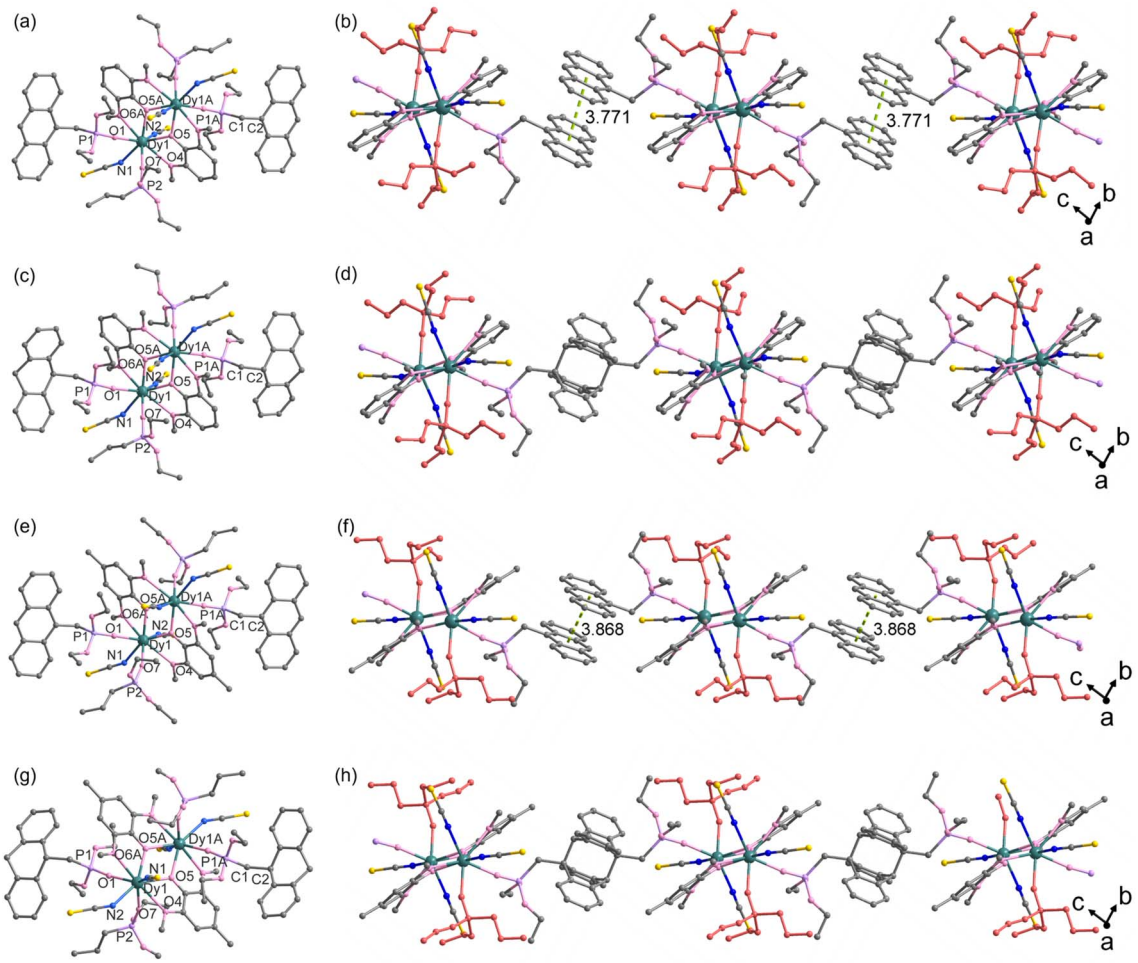

Fig. 1 (a) The molecule structure and (b) 1D supramolecular chain of **1**. (c) The building unit and (d) 1D chain in structure **1UV**. (e) The molecule structure and (f) 1D supramolecular chain of **2**. (g) The building unit and (h) 1D chain in structure **2UV**. The DEPP ligands are highlighted by red colour.

the phenolic oxygen bridges slightly reduces from 3.872 Å in **1** to 3.833 Å in **2**, but the shortest intermolecular Dy···Dy distance of **2** is slightly increased (8.605 *vs.* 8. 566 Å in **1**). It is worth noting that the minor change in the bridging ligand poses distinct influences on the stacking pattern of anthracene groups. The centre-to-centre (d_{cc}) and plane-to-plane (d_{pp}) distances in **2** are larger than those in **1** (3.868 and 3.503 Å *vs.* 3.773 and 3.443 Å in **1**) (Table 1 and Fig. 1f). The slip angle of the π–π interacting anthracene groups in **2** is also larger than that in **1** (24.6° *vs.* 19.7° in **1**). We expect that these structural differences will affect the photophysical and magnetic properties of the two complexes (*vide infra*). Nevertheless, the face-to-face π–π interacting anthracene units in both **1** and **2** satisfy the Schmidt's rule for photocycloaddition reaction.[38]

Photophysical and photochemical properties of 1 and 2

To investigate the photophysical properties of compounds **1** and **2**, we first measured their UV-vis diffuse reflectance spectra in the solid state. Both exhibit strong and broad bands in the 200–600 nm range (Fig. S4), attributed to the π* ← π transition of the anthracene ligand. Additionally, a weak peak was observed at 754 nm for both complexes, which is assigned to the f–f transition from the ground state $^6H_{15/2}$ to the excited states $^6F_{3/2}$ and $^6F_{5/2}$ of the Dy^{3+} ion.[39]

We then recorded the photoluminescence (PL) spectra of **1** and **2**. Both exhibited bright yellow luminescence. Upon excitation at 365 nm, compound **1** shows a broad and strong emission band peaking at 555 nm with a lifetime of 55.2 ns and a quantum yield of 5.09% (Fig. 2a). This band was originated from the excimer emission due to the presence of the face-to-face π–π interacting anthracene rings.[35,40] Interestingly, although compound **2** displays a similar emission profile, the emission peak is markedly blue-shifted to 520 nm (Fig. 2b). This blue-shift should be related to its structural difference compared to **1**. As mentioned above, the plane-to-plane spacing and slip angle of the anthracene pairs in **2** are larger than those in **1** (3.503 Å and 24.6° in **2** *vs.* 3.443 Å and 19.7° in **1**). Therefore, we expect a weaker electronic coupling and hence a higher energy of the excimer state,[41] a shorter emission lifetime (14.4 ns) and a lower quantum yield (4.96%) for **2** compared to those for **1**.[42]

Since the stacking pattern of the anthracene pairs in **1** and **2** is consistent with the Schmidt's rule for photocycloaddition reactions, we next investigated their photochemical properties. Fig. 3a shows the PL spectra of **1** irradiated under 395 nm UV light (LED, IUVOT 50 W) for different times. It is obvious that the intensity of excimer emission at 555 nm decreases with the increase of irradiation time. Meanwhile, after 2 min of irradiation, new peaks at 424 nm and 445 nm are clearly seen, and their intensities increase with irradiation time. These two peaks are assigned to the π* → π transitions of dianthracene,[35] implying the occurrence of photocycloaddition for compound **1**. The emission profile becomes constant after 15 min of irradiation. Impressively, the photochemical reaction is associated with a pronounced emission colour change from yellow-green (CIE 1931 coordinates (0.40, 0.53)) to blue-white (CIE 1931 coordinates (0.27, 0.35)) (Fig. 3b).

The photocycloaddition reaction is also observed for compound **2**. However, in this case, the intensity decrease of the excimer emission is less pronounced than that of compound **1**. More interestingly, the peak wavelength shows a redshift upon light irradiation from 520 nm before irradiation to 535 nm after irradiation for 20 min (Fig. 3c). According to the structural description, the anthracene pair in **2** has a larger slip angle and plane-to-plane spacing than compound **1**. We hypothesize that when exposed to UV light, the photochemical reaction first occurs at the surface and then rapidly advances to the interior of the crystal.[40] The formation of dianthracene at the beginning of the reaction may affect the way the unreacted anthracene pairs are stacked, causing a slight decrease in their slip angle, which in turn leads to a redshift of the excimer emission peak.[43] In addition, the newly emerged peaks at 422 and 445 nm are relatively weak. As a result, the emission colour change for compound **2** before and after UV irradiation is not as significant as compound **1**, as evidenced by the CIE 1931 coordinates from (0.29, 0.52) to (0.31, 0.50) (Fig. 3d).

To obtain pure phases of the photocycloaddition reaction products for physical property measurements, we irradiated 20 mg of the crystal samples of **1** and **2** separately with 395 nm UV light for 12 h. The products are named as **1UV** and **2UV**, respectively. Their PXRD patterns matched well with those

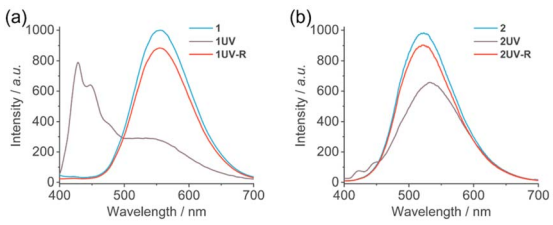

Fig. 2 PL spectra excited at 365 nm for **1**, **1UV** and **1UV-R** (a), and **2**, **2UV** and **2UV-R** (b).

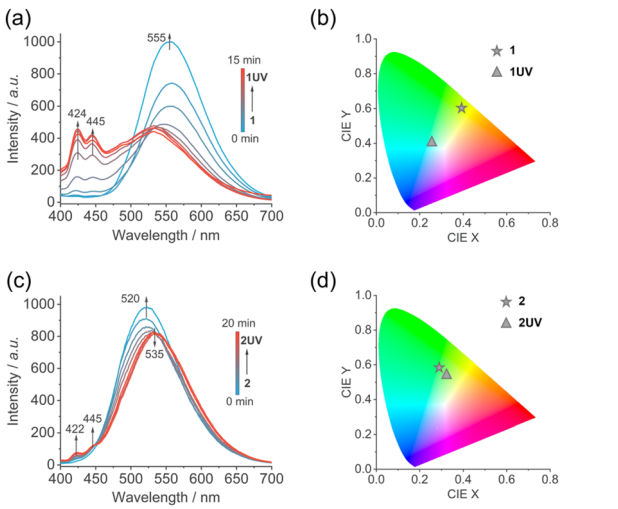

Fig. 3 (a and c) PL spectra for **1** (a) and **2** (c) with irradiation time upon 395 nm UV-light irradiation (λ_{ex} = 365 nm); (b and d) the CIE graphs of **1**, **1UV** (b) and **2**, **2UV** (d).

simulated from the single crystal data of **1UV** and **2UV** (Fig. S5 and S6). We measured the infrared (IR) spectra of **1UV** and **2UV** in comparison with those of **1** and **2**. As shown in Fig. S7 and S8, the vibrational absorption peaks of depma in **1** (810 cm^{-1}) and **2** (732 cm^{-1}) disappeared, while those of $depma_2$ emerged in **1UV** (1225, 876, and 686 cm^{-1}) and **2UV** (1281, 885, 693 cm^{-1}). To examine quantitatively the yields of photocycloaddition reactions of **1** and **2**, we further measured ^{1}H NMR spectra of **1UV** and **2UV**. The peaks at 7.5–8.6 ppm and 6.7–7.3 ppm are assigned to depma and $depma_2$,[25,44] respectively (Fig. S9 and S10). By integrating the peaks of anthracene and dianthracene, we can estimate the photochemical reaction yields of **1** and **2** to be 99.9% and 93.2%, respectively, indicating that these photocycloaddition reactions are almost complete for the two compounds. Fig. 2 shows the PL spectra of **1UV** and **2UV**. For **2UV**, we still observe a significant broad band around 550 nm, attributed to the presence of a small amount of un-dimerized anthracene pair.[45] To determine whether the reaction can be reversed under illumination, we took **1UV** as an example and irradiated it with 254 nm light for 12 h. The ^{1}H NMR result showed that only 2.7% of **1UV** was reversed to **1** (Fig. S11). Obviously, the complete de-dimerization of **1UV** induced by light is not feasible.

To gain insight of the structures of photocycloaddition reaction products, we irradiated single crystals of **1** and **2** under 395 nm light (183 mW cm^{-2}) for 30 min. Both exhibited SC–SC structural transformation to form 1D coordination polymers $[Dy_2(SCN)_4L_2(depma_2)(DEPP)_2]_n$ (**1UV**) (Fig. 1c and d) and $[Dy_2(SCN)_4(L^{Me})_2(depma_2)(DEPP)_2]_n$ (**2UV**), respectively (Fig. 1g and h). Structural analyses revealed that **1UV** and **2UV** crystallized in the triclinic $P\bar{1}$ space group, similar to those of **1** and **2** (Table 1). As expected, the light-induced structural transformation leads to changes in Dy–O(N) bond lengths and O(N)-Dy-O(N) angles (Tables S6 and S7). However, these changes are quite small compared to the other known Dy-anthracene complexes. The coordination geometries of Dy^{III} ions in **1UV** and **2UV** can still be best described as the Biaugmented trigonal prism J50, but the deviations are slightly different from their original ones (CShM = 2.700 for **1UV** *vs.* 2.588 for **1**, 2.565 for **2UV** *vs.* 2.669 for **2**) (Table S3). The most significant change is found for the face-to-face stacking anthracene pairs. The central C2···C9A distances are remarkably shortened from 3.771 Å to 1.669 Å for **1**, and from 3.860 Å to 1.689 Å for **2**. Interestingly, the C2–C9A bond length in **1UV** (1.669 Å) is shorter than that in **2UV** (1.689 Å), indicating that the *in situ* formed dianthracene in **1UV** could be more stable than that in **2UV**. The different stability of the *in situ* formed dianthracene in **1UV** and **2UV** is also reflected by their de-dimerization temperatures.

Thermally induced de-dimerization of dianthracene in 1UV and 2UV

Thermogravimetric analysis (TGA) revealed that compounds **1UV** and **2UV** did not show weight loss below 180 °C (Fig. 4a and c). However, the DSC curves showed broad exothermic peaks in the temperature ranges of 55–95 °C and 45–95 °C for **1UV** and **2UV**, respectively (Fig. 4b and d), corresponding to the de-

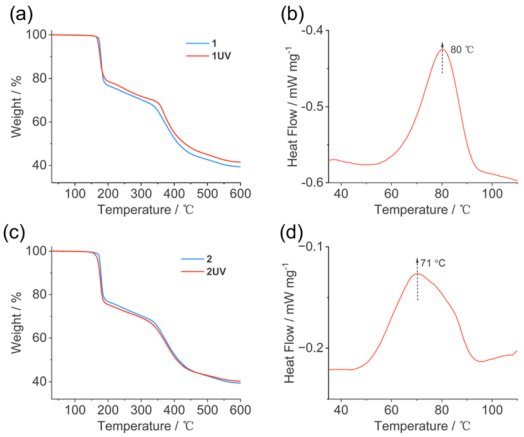

Fig. 4 (a and c) The TG curves of compound **1**, **1UV** (a) and **2**, **2UV** (c); (b and d) the DSC curves of compound **1UV** (b) and **2UV** (d).

dimerization of dianthracene ligands. The maximum of the exothermic peak, defined as the de-dimerization temperature, appeared at 80 °C for **1UV** and 71 °C for **2UV**. The enthalpy changes (ΔH) are estimated to be −49.8 kJ mol^{-1} for **1UV** and −53.7 kJ mol^{-1} for **2UV**. To obtain fully de-dimerized products, we kept **1UV** at 80 °C for 10 min or **2UV** at 71 °C for 10 min, the resulting products are named as **1UV-R** and **2UV-R**. The PXRD, PL, IR, and UV-vis diffuse reflectance spectra of **1UV-R** and **2UV-R** are identical to those of **1** and **2**, respectively (Fig. 2 and S4–S8), indicating that the original compounds **1** and **2** were fully recovered by heating **1UV** and **2UV**. Apparently, the photocycloaddition reactions of **1** and **2** were reversible, which was also supported by single crystal structural analysis. To determine whether the SC–SC structural transformation can be repeated, we conducted five cycles of irradiation/heating on **1** using the same crystal. We found cracks in the obtained crystal, but the crystal fragments can be used for single-crystal structural analysis (Fig. S12). For compound **2**, we repeated the irradiation/heating process for three cycles and found that the crystal did not fracture, still suitable for single-crystal structural analysis (Fig. S13).

We noticed that the de-dimerization temperatures of compounds **1UV** and **2UV** are significantly lower than those for the other related compounds $[Dy_2(SCN)_4L_2(depma_2)(H_2O)_2]_n$ (**3UV**, 100 °C),[32] $[Dy_2(SCN)_4L_2(dmpma_2)(H_2O)_2]_n$ (**4UV**, 100 °C),[32] and $[Dy_2(SCN)_4L_2(dmpma_2)(dmpma_2)_2]_n$ (**5UV**, 124 °C),[33] where dmpma represents 9-dimethyl-phosphonomethylanthracene and $dmpma_2$ is the photo-dimerized dmpma. Compounds **3UV**, **4UV** and **5UV** are photocycloaddition products of $[Dy_2(SCN)_4L_2(depma)_2(H_2O)_2]$ (**3**), $[Dy_2(SCN)_4L_2(dmpma)_2(H_2O)_2]$ (**4**), and $[Dy_2(SCN)_4L_2(dmpma)_4]$ (**5**), respectively. Considering that all these compounds have similar binuclear core structures, the difference in de-dimerization temperatures of **1UV**–**5UV** must be related to the stability of the dianthracene units formed *in situ* in the solid state. We hypothesize that the stability of dianthracene is highly dependent on the stacking pattern of anthracene pairs in its original compounds **1**–**5** (Fig. 1 and S14). When the two anthracene groups are arranged in parallel, the

stacking pattern can be characterized by two key parameters, *i.e.*, the slip angle (θ) and plane-to-plane distance (d_{pp}). Anthracene pairs with a larger slip angle and d_{pp} value are expected to result in dianthracene units with less stability.

Table 2 summarizes some of the structural parameters of the anthracene pairs in **1–5** and their corresponding de-dimerization temperatures for the photocycloaddition products **1UV–5UV**. Clearly, the de-dimerization temperatures follow the order: **2UV** (71 °C) < **1UV** (80 °C) < **3UV** (100 °C), **4UV** (100 °C) < **5UV** (124 °C). Among these five compounds, **2UV** has the lowest de-dimerization temperature (71 °C), while its corresponding anthracene pair in the original compound **2** has the largest slip angle (24.6°) and d_{pp} value (3.503 Å). In contrast, compound **5UV** has the highest de-dimerization temperature (124 °C), while its corresponding anthracene pair in the original compound **5** has the smallest slip angle (16.9°) and d_{pp} value (3.355 Å). For compounds **3UV** and **4UV**, although the slip angle of the anthracene pair in **3** (16.9°) is smaller than that in **4** (19.9°), the d_{pp} value in **3** (3.410 Å) is close to that in **4** (3.407 Å). This may explain why the de-dimerization temperature is similar for **3UV** and **4UV** (100 °C). It is noteworthy that the slip angle in compound **1** is close to that in **4** (19.7° in **1** *vs.* 19.9° in **4**), but the d_{pp} value in **1** (3.485 Å) is larger than that in **4** (3.407 Å). As a result, the de-dimerization temperature of **1UV** (80 °C) is much lower than that of **4UV** (100 °C). All these results validate the above hypothesis that the stability of the *in situ* formed dianthracene depends strongly on the slip angle and d_{pp} values of the anthracene pair, while the plane-to-plane distance (d_{pp}) seems to be more important.

When photocycloaddition of π–π interacting anthracene pair in Dy-anthracene complexes occurs, we expected that the Dy···Dy distance over the dianthracene bridge would change significantly. This is indeed the case for compounds **3** and **5** whose distances are shortened by 0.104 Å and 1.050 Å, respectively. Interestingly, the change in the Dy···Dy distance in compound **2** (0.050 Å) is much less significant, whereas this change is hardly visible in compound **1** (0.004 Å). The fact that the metal ion spacing remains essentially unchanged before and after photocycloaddition favours, on the one hand, the ability of the structural transformation to proceed in a single-crystal-to-single-crystal fashion, while on the other hand, it leads to a decrease in the stability of the resulting dianthracene product. As a result, the ∠P1–C1–C2 angles after photocycloaddition are significantly increased compared to those in the initial samples (Table 2), deviating markedly from the characteristic angle of sp^3-hybridized carbon atoms (109.5°). However, we note that the ∠P1–C1–C2 angle for **1UV** (125.9°) is larger than that for **2UV** (124.7°), but the former has a higher de-dimerization temperature. Clearly, the extent to which this ∠P1–C1–C2 angle deviates from 109.5° is less important in contributing to dianthracene stability than the anthracene stacking pattern discussed above.

The fact that the dianthracene in **1UV** and **2UV** can dissociate at temperatures well below 100 °C demonstrates the possibility to regulate the de-dimerization temperature of the *in situ* formed dianthracene by introducing a suitable co-ligand, which is DEPP in the present cases. Moreover, compounds **1UV** and **2UV** have very similar structures except for the additional methyl group in the ligand 2,6-dimethoxyphenol in **2UV**, but their de-dimerization temperatures are different by 9 °C. This result implies that the de-dimerization temperature of *in situ* formed Ln-dianthracene compounds can also be regulated by ligand modification. To the best of our knowledge, the de-dimerization temperature of **2UV** (71 °C) is the lowest among the known metal–dianthracene complexes.

Photocycloaddition reaction of 1 at different temperatures

The fact that de-dimerization of **1UV** and **2UV** can be observed at temperatures below 80 °C opens the possibility of rapid switching of the PL properties of compounds **1** and **2** above room temperature. On the one hand, elevated temperature may make excited state molecules more susceptible to structural relaxation, thus accelerating the photocycloaddition reaction rate. On the other hand, elevated temperatures also increase the de-dimerization rate of the photocycloaddition products formed *in situ*. Thus, the PL spectra as a function of irradiation time at elevated temperatures is the result of competing photodimerization and de-dimerization processes. To investigate the

Table 2 Comparison of the de-dimerization temperature and related structural parameters of dysprosium anthracene-based complexes

Compound	d_{CC}[a]/Å	d_{pp}[b]/Å	d_{C2-C9A}[c]/Å	Slip angle[d]/°	$d_{Dy\cdots Dy}$[e]	∠P1–C1–C2/°	T_d[f]/°C	Ref.
1	3.771	3.485	3.773	19.68	15.617	114.5		This work
1UV			1.669		15.613	125.9	80 (55–95)	This work
2	3.868	3.503	3.860	24.60	15.607	115.1		This work
2UV			1.689		15.657	124.7	71 (45–95)	This work
3	3.690	3.410	3.700	16.88	14.671	114.6		21
3UV			1.689		14.775	121.6	100 (92–105)	21
4	3.652	3.407	3.654	19.91	14.592	114.6		21
4UV			n.a.		n.a.	n.a.	100 (90–105)	21
5	3.688	3.355	3.687	16.91	16.783	115.3		22
5UV			1.635		15.733	124.9	124 (112–133)	22

[a] The centre-to-centre distance. [b] Plane-to-plane distance. [c] The central C2–C9A distance of the π–π interacting anthracene pair. [d] The angle between the centroid–centroid line and the vertical line in anthracene. [e] The Dy···Dy distance over the anthracene pair of dianthracene bridge. [f] The de-dimerization temperature. The values in the parentheses are the temperature ranges of the exothermic peaks determined by DSC curves; n.a. means not available.

effect of temperature on photochemical reactions, compound **1** was chosen as a representative for detailed study because it showed significant spectral changes before and after photocycloaddition reaction.

We selected single crystals of **1** and studied the PL spectra after irradiation for different times at temperatures 20–120 °C using a home-built fluorescence microscope. Due to the limited light sources available for this instrument, we used 375 nm laser for UV irradiation and excitation with initial power of 21.75 μW and power density of 3000 mW cm^{-2}. All measurements were conducted at the same position on the crystal to ensure *in situ* testing conditions.

Fig. 5 shows the real-time PL spectral change and the normalized selected PL spectra at different times of compound **1** at 20–120 °C. It is clear that in all cases the peak intensity at 550 nm, which corresponds to the excimer emission of anthracene pair, progressively decreases. While the peak intensity at 425 nm, which corresponds to the emission of dianthracene, increases with prolonged illumination time. The results indicate that photodimerization reaction still occurs at 80 °C and above. It is worth noting that the peak of the excimer emission occurs at 550 nm instead of 555 nm due to the different instruments used to measure the PL spectra of single crystals and bulk samples. In addition, we observed the emergence of weak peaks in the near infrared (NIR) region of 800–850 nm, with the maximum at 833 nm, which increases with irradiation time. This peak is attributed to the $^4F_{9/2} \rightarrow {}^6F_{9/2}$, $^6H_{7/2}$ transitions of the Dy^{3+} ions.[39,46] Obviously, the dianthracene formed *in situ* is able to transfer energy to and sensitize the Dy^{3+} ions,[23,47] thereby inducing the NIR luminescence of the Dy^{3+} ions. The f–f transitions in the visible region cannot be identified.

We further attempted to determine the rate constants of the compound **1**. We note that few kinetic studies of anthracene photodimerization reactions have been reported in the literature.[48–53] Infrared spectroscopy is generally used to follow

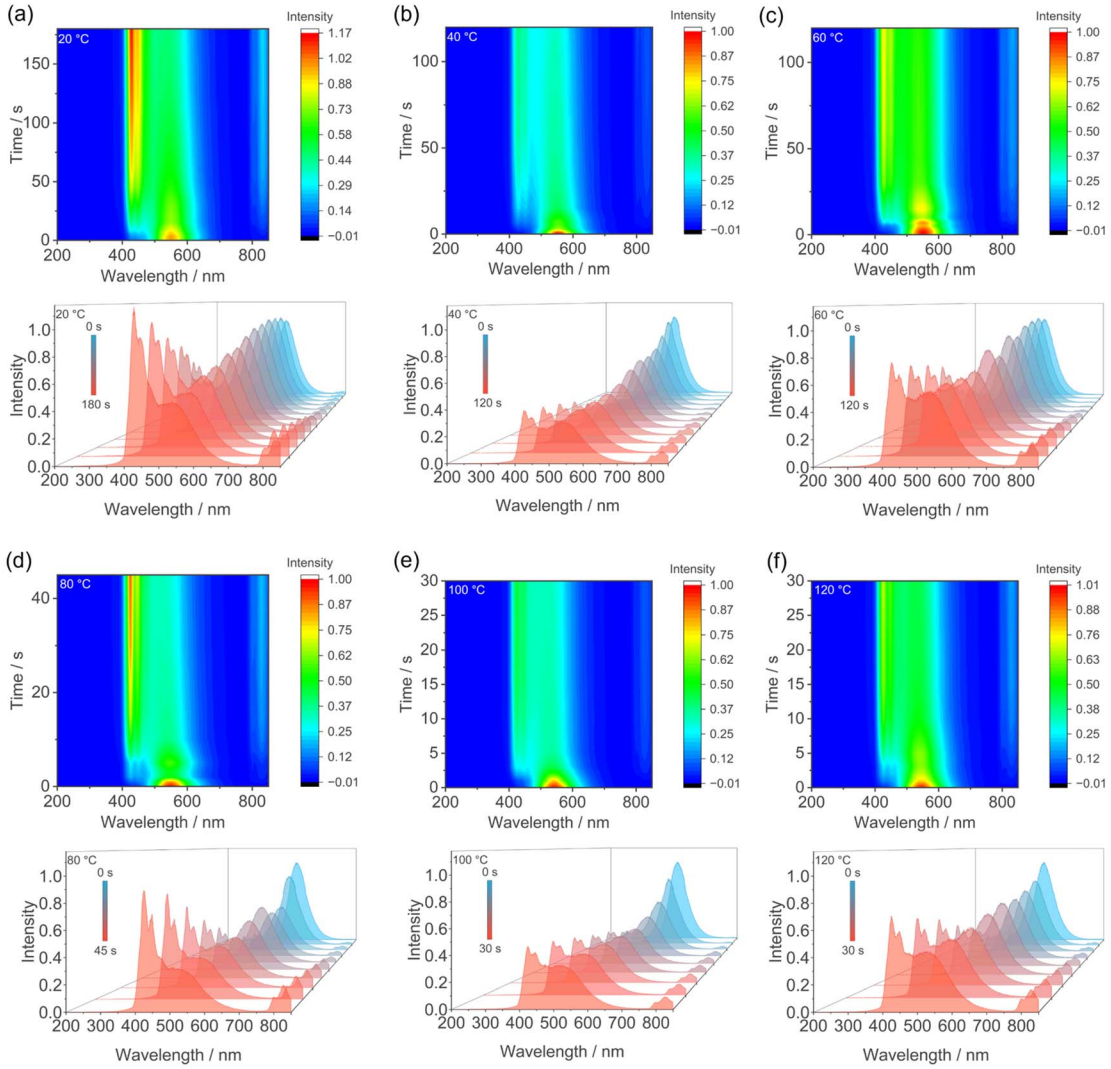

Fig. 5 The real-time PL spectral change (up) and the normalized selected PL spectra at different times (down) of compound **1** at 20 °C (a), 40 °C (b), 60 °C (c), 80 °C (d), 100 °C (e), and 120 °C (f). The 375 nm laser was used for UV irradiation and excitation.

the progress of the reaction in the solid phase,[35,52] or absorption spectroscopy is used to study the reactions in the solution phase.[48,49] As far as we are aware, there is only one reported case of using fluorescence spectroscopy to study the kinetics of anthracene photodimerization reaction at room temperature.[53]

We first monitored the intensity change of the peak at 425 nm. The conversion ratio was calculated using the equation $y = |I - I_0|/\Delta I$, where I and I_0 represent the real-time and initial PL intensity, respectively, and ΔI represents the difference between the initial and final intensity when the PL profile becomes constant. We observed that $\ln(1 - y)$ exhibited an approximately linear relationship with irradiation time under different temperatures, which is consistent with first-order reaction kinetics (Fig. S15). Similar kinetic behaviour has been observed in a few other anthracene-based compounds.[54–56] The $\ln(1 - y)$ *vs.* time plots were well fitted by using the first-order logarithmic equation $\ln(1 - y) = -kt$, where k is the rate constant, to obtain the reaction rate constant k at temperatures in range of 20–120 °C (Table 3). It is clear that the k value increases with increasing temperature until 100 °C, above which the k value decreases with temperature (Fig. 6a). The same conclusion can be obtained by fitting the data using the intensity change of the peak at 550 nm (Fig. 6a, S16 and Table S8). According to the Arrhenius equation $k = A\exp(-E_a/RT)$, the activation energy can be derived by linear fitting of the $\ln k$ *vs.* $1/T$ plot in range of 20 to 100 °C, which is 22.13 ± 3.02 kJ mol^{-1} (based on the 420 nm peak) or 25.72 ± 4.19 kJ mol^{-1} (based on the 550 nm peak) (Fig. 6b). As far as we know, the activation energy of anthracene photocycloaddition reaction has not been reported before. However, Chen and co-workers recently conducted theoretical studies on the photophysical and photochemical properties of mononuclear compounds Ln(depma)(hmpa)$_2$(NO$_3$)$_3$ (**1-Ln**, Ln = Eu, Tb).[47] They found that the calculated barriers for the ligand-centred intersystem crossing (ISC) $^1\pi\pi^* \rightarrow {}^3\pi\pi^*$ transition, which led to the [4 + 4] photocycloaddition reaction, were 8.8 kcal mol^{-1} (36.78 kJ mol^{-1}) for **1-Eu** and 9.1 kcal mol^{-1} (38.04 kJ mol^{-1}) for **1-Tb**. These calculated values are relatively close to those observed for compound **1**.

As already mentioned, the PL spectra obtained after irradiation at higher temperatures are the result of competing photodimerization and de-dimerization processes. The latter should be solely due to temperature effects, since irradiation of anthracene with a 375 nm laser leads only to dimerization without the reverse process of de-dimerization.[57] The DSC curve of **1UV** revealed that the de-dimerization process started at about 55 °C, reached a maximum at 80 °C and ended at 95 °C. Kinetics studies have shown that the rate of photocycloaddition reaction of **1** reaches a maximum at 100 °C and decreases above this temperature. The results indicate that it is still possible for a photocycloaddition reaction of anthracene to occur when the temperature for complete de-dimerization is attained. To verify this conclusion, compound **1** was placed on a hot plate and irradiated with 395 nm UV light (100 mW cm^{-2}) for 2 h at constant temperatures of 60 °C, 80 °C, and 100 °C. The NMR results showed that the reaction conversion rate decreased with increasing temperature, but dimerized products were still formed even at 100 °C (Fig. S17–S19). To the best of our knowledge, although a few studies of the kinetics of the anthracene photocycloaddition reaction at or below room temperature have been reported,[35,49,57,58] similar kinetic studies above room temperature have never been documented in the literature. This finding is important for the selection of a suitable temperature for rapid structural and photoluminescence switching of anthracene-based systems.

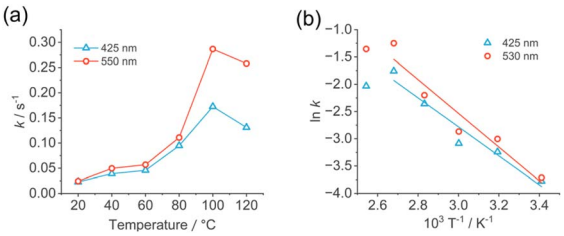

Fig. 6 (a) The k *vs.* T plots for compound **1**. The solid lines are eye-guided. (b) The $\ln k$ *vs.* $1/T$ plots for **1**. The solid lines are best fits.

Light-induced changes in magnetic properties of 1 and 2

Structural analyses have demonstrated that photocycloaddition reaction causes slight changes in the bond lengths and angles of the Dy^{3+} ions in **1** and **2**. These changes in coordination environments should affect their magnetic properties. Fig. S20 shows the temperature dependent magnetic susceptibilities of the two compounds before and after photocycloaddition. At 300 K, the $\chi_M T$ values are 28.50 and 28.27 cm^3 K mol^{-1} for **1** and **2**, respectively, which are consistent with the expected value of two isolated Dy^{III} ions (28.34 cm^3 K mol^{-1}, $^6H_{15/2}$, $S = 5/2$, $L = 5$, $g_J = 4/3$). As the temperature decreases, the $\chi_M T$ values remain nearly constant until 100 K, below which they decrease slowly to reach the minimum values of 27.40 and 28.06 cm^3 K mol^{-1} at 45 K for **1** and **2**, respectively, attributed to the depopulation of Stark sublevels. The rapid increase of the $\chi_M T$ values below 45 K suggest the existence of ferromagnetic interaction between the Dy^{III} ions. Similar phenomenon was observed in some other binuclear Dy$_2$O$_2$ complexes with phenoxy bridges.[59–61] The field dependent magnetization curves were also measured at different temperatures. The magnetization (M) values at 2 K and 70 kOe are 10.81 Nβ for **1** and 10.55 Nβ for **2** (Fig. S21 and S22), which are lower than the theoretical saturation values of 20 Nβ

Table 3 The rate constant obtained at different temperatures by fitting the intensity data at 425 nm (k_1) and 550 nm (k_2)

T/°C	20	40	60	80	100	120
k_1/s^{-1}	0.023(1)	0.039(1)	0.046(2)	0.095(2)	0.172(9)	0.131(8)
k_2/s^{-1}	0.024(1)	0.050(6)	0.057(5)	0.111(16)	0.287(47)	0.258(28)

for two Dy^{III} ions. This may be due to the presence of significant magnetic anisotropy and/or low-lying excited states of the Dy^{III} ions in compounds **1** and **2**.[62] Interestingly, the $\chi_M T$ *vs.* T and M *vs.* H curves of **1UV** and **2UV** almost overlap the curves for their counterparts prior to UV irradiation (Fig. S20 and S23).

Significant changes are found in the magnetic dynamics. For both compounds **1** and **2**, we observed frequency-dependent in-phase (χ_M') and out of phase (χ_M'') magnetic susceptibilities under zero dc field (Fig. 7 and S24), which is characteristic of single-molecule magnet (SMM) behaviour. The Cole–Cole plots can be fitted by the generalized Debye model to extract the relaxation time (τ) (Fig. S25).[63] The distribution coefficient (α) values are found to be in the ranges of 0.27–0.47 for **1** and 0.19–0.41 for **2**, respectively (Tables S8 and S9), indicating the existence of a broad relaxation time distribution. Fig. 7c and f show the $\ln\tau$ *vs.* T^{-1} plots for both compounds. For **1**, the linear relationship between 4 K and 6 K indicates that the relaxation is dominated by the Orbach process, while below 4 K, a nonlinear relationship is observed, indicating the domination of relaxation by Raman processes. Similar profile is observed for compound **2**. Therefore, the plot of $\ln\tau$ *vs.* T^{-1} can be fitted by using the eqn (1) containing Raman and Orbach processes, where U_{eff} is the effective energy barrier.

$$\tau^{-1} = CT^n + {\tau_0}^{-1}\exp(-U_{eff}/kT) \quad (1)$$

The best fits gave parameters $U_{eff} = 57(2)$ K, $\tau_0 = 10^{-7.8(2)}$ s, $n = 2.78(9)$, and $C = 2.64(23)$ $K^{-2.78}$ s^{-1} for compound **1**, and $U_{eff} = 78(2)$ K, $\tau_0 = 10^{-8.6(1)}$ s, $n = 2.52(8)$, and $C = 0.42(4)$ $K^{-2.52}$ s^{-1} for compound **2** (Table 4).

Notably, the effective energy barrier of **2** (78 K) is higher than that of **1** (57 K). According to the structural description, the main difference between **1** and **2** is that the latter has an additional methyl group in the bridging 2,6-dimethoxyphenol ligand. This difference causes slight changes in the coordination environment of the Dy^{III} ion. Compared to those in **1**, the Dy1-O5 and Dy1-O5A bond lengths and Dy1···Dy1A distance in **2** are shorter [2.250(5), 2.284(5) and 3.833(1) Å *vs.* 2.295(3), 2.297(3) and 3.871(1) Å in **1**], but the Dy1-O5-Dy1A angle in **2** is larger [115.4(2)° *vs.* 114.9(1)° in **1**]. Previous studies on the related compound $[Dy_2(SCN)_4L_2(dmpma)_4]$ (**5**) have demonstrated that the magnetic axes lie in the Dy_2O_2 plane along the Dy1–N1 bond (Fig. 8).[33] Given that the Dy1–N1 bond length is nearly the same in the two structures and most of the equatorial Dy1–O(N) bond lengths in **2** are slightly shorter than those in **1** (Table 1), it is difficult to judge which structural factor plays the key role in enhancing the SMM performance of **2**. Nevertheless, the effective energy barriers of **1** and **2** are comparable to those

Table 4 Magnetic parameters for compounds **1**, **1UV**, **2** and **2UV** derived by fitting the $\ln\tau^{-1}$ *vs.* T plots to eqn (1)

	U_{eff}/K	τ_0/s	C/K^{-n} s^{-1}	n
1	57	1.74×10^{-8}	2.64	2.78
1UV	94	3.30×10^{-8}	0.49	2.99
2	78	2.60×10^{-9}	0.42	2.52
2UV	84	6.06×10^{-9}	0.27	2.80

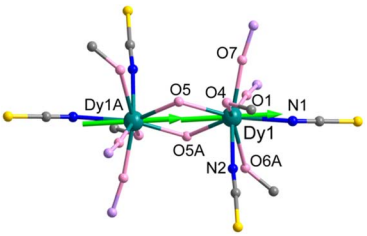

Fig. 8 The coordination environment of the dysprosium ion in **1**. The green arrow represents the orientation of the local main magnetic axis.

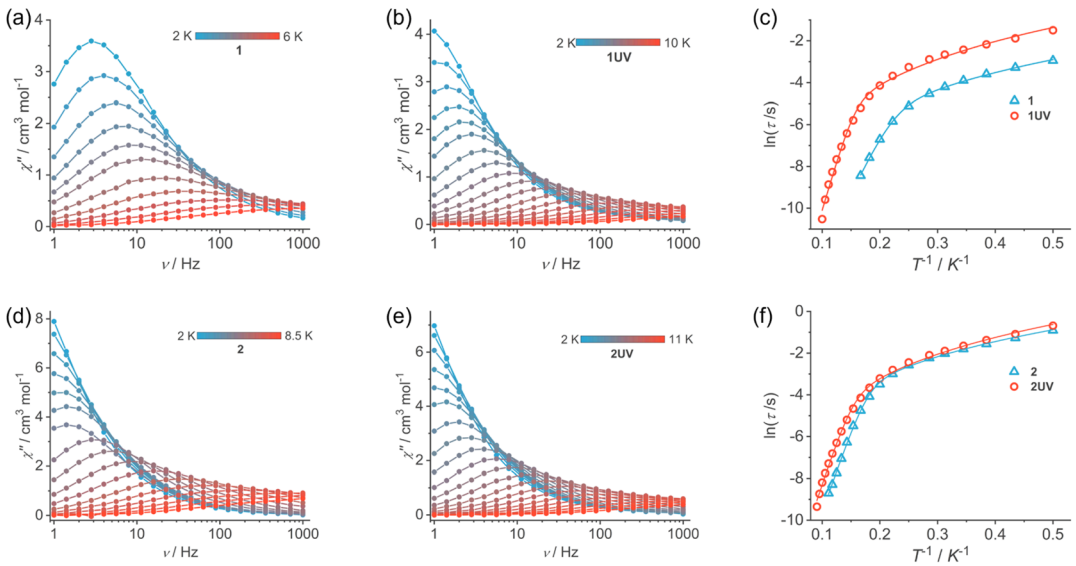

Fig. 7 (a, b, d and e) The out-of-phase ac susceptibilities for **1** (a), **1UV** (b), **2** (d) and **2UV** (e); (c and f) the plot of $\ln\tau$ *vs.* T^{-1} for **1**, **1UV** (c) and **2**, **2UV** (f).

of compounds **5** (55.9 K)[33] and $[Dy_2(L^1)_2(L^2)_2(CH_3OH)_2]$ (L^1 = [((2-hydroxyphenyl)imino)methyl]phenol, L^2 = 2,6-dimethoxyphenol) (69.0 K),[64] but smaller than those of compounds **3** (110.8 K),[32] **4** (117.7 K),[32] $[Dy_2(NO_3)_4(H_2O)_2(L)_2]_2\cdot CH_3CN$ (220.1 K),[65] and $[Dy_2(DMOAP)_2(DBM)_4]_2\cdot CHCl_3$ (DMOAP = syringaldehyde, DBM = 1,3-diphenylpropane-1,3-dione) (175.2 K)[66] which contain similar Dy_2O_2 dimer cores.

After light irradiation, the product **1UV** shows magnetic dynamics different from that of **1**, with the peaks in the χ''_M *vs.* ν curves appearing at higher frequencies. However, the χ''_M *vs.* ν profiles for **2UV** are very similar to those for **2**. The $\ln\tau$ *vs.* T^{-1} curves can again be fitted by using the eqn (1), resulting in parameters $U_{eff} = 94(5)$ K, $\tau_0 = 10^{-8.5(5)}$ s, $n = 2.99(18)$, and $C = 0.49(11)$ $K^{-2.99}$ s^{-1} for **1UV**, and $U_{eff} = 84(3)$ K, $\tau_0 = 10^{-8.2(2)}$ s, $n = 2.80(12)$, and $C = 0.27(4)$ $K^{-2.80}$ s^{-1} for **2UV**, respectively (Table 4). Compared to **1**, the effective energy barrier of **1UV** is increased by 37 K. We notice that the Dy1–O distances in **1** are either slightly shortened or elongated after light irradiation (Table 1). The most significant change is found for the Dy1–N bond lengths. The axial Dy1–N1 bond length is similar [2.388(5) Å in **1UV** *vs.* 2.392(5) Å in **1**] while the equatorial Dy1–N2 distance is elongated [2.398(5) Å in **1UV** *vs.* 2.379(4) Å in **1**], which may contribute to the increase of the U_{eff} value of **1UV**. Surprisingly, the energy barrier of **2** remains almost the same before and after photocycloaddition. Structural analysis revealed that all Dy1–O(N) bond lengths in **2UV** are slightly expanded except for the axial Dy1–N1 which is slightly shortened [2.380(6) Å in **2UV** *vs.* 2.388(7) Å in **2**] (Table 1). As a result, the overall magnetic anisotropy of **2UV** could be similar to **2** and, therefore, the similar U_{eff} values.

Another interesting observation is the change in the Raman index value. According to the Debye model theory, the theoretical value of Raman index for Kramers ion system should be $n = 9$.[67] However, the presence of low-energy phonon vibrations in the system can cause the Debye model to deviate, and the Raman index usually falls within the range of 2–6.[68] This is indeed the case for compounds **1** and **2** as well as their photocycloaddition products which have the Raman index of 2.52–2.99. The n values of **1UV** ($n = 2.99$) and **2UV** ($n = 2.80$) are slightly higher than those of **1** ($n = 2.78$) and **2** ($n = 2.52$), attributed to the formation of 1D coordination polymers.

$$\tau^{-1} = A^{-1}\exp\left(-\frac{\hbar\omega}{kT}\right) + {\tau_0}^{-1}\exp\left(-\frac{-U_{eff}}{kT}\right) \quad (2)$$

By fitting the $\ln\tau^{-1}$ *vs.* T plots to Raman process in the low-temperature region using equation $\tau \sim [\exp(\hbar\omega/k_BT)]$,[69] we obtained the vibration energies ($\hbar\omega$) of 3.88 cm^{-1} for **1**, 4.76 cm^{-1} for **1UV**, 4.25 cm^{-1} for **2**, and 5.21 cm^{-1} for **2UV** (Fig. S26). If the Orbach process is combined, we can use eqn (2) to fit the entire dataset and obtained the energy barriers (U_{eff}) as well as the vibration energies ($\hbar\omega$) (Table S12 and Fig. S27). The U_{eff} values are close to those obtained using eqn (1). While the vibration energies are 4.88 cm^{-1} for **1**, 6.02 cm^{-1} for **1UV**, 5.03 cm^{-1} for **2**, and 6.00 cm^{-1} for **2UV**. Notably, compounds **1** and **2** exhibit a significant increase in vibrational energy after photocycloaddition, indicating that the photocycloaddition reaction effectively suppresses low-energy phonon vibrations.

Theoretical calculations of magnetic properties

Theoretical calculations can reveal the relationship between structure and magnetic properties. Based on the geometries determined by X-ray crystallography, we performed complete-active-space self-consistent field (CASSCF) calculations on individual Dy^{III} fragments in the complexes **1**, **1UV**, **2**, and **2UV** using OpenMolcas[70] and SINGLE_ANISO[71–73] programs (see SI for details). Table S13 lists the calculated energy levels, g (g_x, g_y, g_z) tensors and the dominant m_J values of the lowest eight Kramers doublets (KDs) of each Dy^{III} fragment. The energy gap between the two lowest KDs of **1_Dy1** and **1UV_Dy1** is close, with a similar situation observed for **2_Dy1** and **2UV_Dy1**. In all cases, the ground state is primarily composed of $m_J = \pm 15/2$ states (Table S14), resulting in a small transversal magnetic moment. However, the first excited state KD is significantly populated by multiple m_J states, leading to a large transversal magnetic moment in the first excited state KDs of **1–2UV**.

Fig. S29 illustrates the corresponding magnetisation blocking barriers for the Dy^{III} fragments in **1–2UV**. The transversal magnetic moments in the ground state KDs are all less than $0.5 \times 10^{-1}\mu_B$, thus suppressing the quantum tunnelling of magnetisation (QTM) in the ground states at low temperatures. Notably, the transversal magnetic moments of the four Dy^{III} fragments in the first excited state are 0.79, 0.12×10^1, 0.31 and $0.29\mu_B$, respectively, all exceeding $0.5 \times 10^{-1}\mu_B$. Consequently, rapid QTM is permitted in their first excited state KD. The calculated energy barriers for **1_Dy1**, **1UV_Dy1**, **2_Dy1** and **2UV_Dy1** are 177.3, 185.4, 162.7 and 173.7 cm^{-1}, respectively, which are quite close to each other. The barriers for **1UV_Dy1** and **2UV_Dy1** are slightly higher than those for **1_Dy1** and **2_Dy1**, consistent with experimental findings. Considering the detrimental effects of anharmonic phonons, Raman magnetic relaxation, QTM, *et al.* on energy barriers, experimentally measured energy barriers (U_{eff}) are typically lower than the calculated values.[74–79]

Although the magnetic anisotropy in **1–2UV** primarily originates from individual Dy^{III} ions, Dy^{III}-Dy^{III} interactions still exert a certain influence on its slow magnetic relaxation process. By comparing the calculated and experimentally measured magnetic susceptibility of **1–2UV**, we utilised the POLY_ANISO program[71–73] to fit the exchange coupling constant $\tilde{J}_{exch}$ and intermolecular interaction zJ'. The parameters in Table 5 were calculated based on Dy^{III} ions with a pseudospin of $\tilde{S}_{Dy} = 1/2$. The magnetic susceptibility fitting includes total coupling parameters $\tilde{J}_{total}$ (dipolar and exchange). Fig. S30 displays the calculated and experimental χ_MT *vs.* T curves for complexes **1–2UV**, with all fitting results showing good agreement with experimental data across the entire temperature range.

The positive $\tilde{J}_{total}$ obtained from Lines model[80] indicate that the Dy^{III}–Dy^{III} interactions within the **1–2UV** complexes are ferromagnetic, which agrees with the experimental results. Surprisingly, however, the total and exchange coupling constants for these four compounds are almost identical. This may be attributed to the minimal variations in structural parameters among them, which collectively exerted negligible influence on the intramolecular magnetic interactions within

Table 5 The fitted exchange coupling constant ($\tilde{J}_{exch}$), calculated dipole–dipole interaction ($\tilde{J}_{dip}$) and total constant ($\tilde{J}_{total}$) between magnetic centre ions in **1–2UV**. The fitted intermolecular interactions (zJ') in compounds **1**, **1UV**, **2** and **2UV** are −0.005, −0.01, −0.001 and −0.003 cm^{-1}, respectively

	1	1UV	2	2UV
$\tilde{J}_{exch}$	2.5	2.5	2.5	2.5
$\tilde{J}_{dip}$	5.9	5.8	5.8	5.8
$\tilde{J}_{total}$	8.4	8.3	8.3	8.3

the dimer. We present the exchange energies, the energy differences between each exchange doublet Δ_t and the main values of the g_z for the lowest two exchange doublets of **1–2UV**. As shown in Table S15, the g_z values for the ground exchange states of compounds **1**, **1UV**, **2** and **2UV** are 39.671, 39.679, 39.395 and 39.711, respectively, further confirming that the Dy^{III}–Dy^{III} interactions in **1–2UV** are all ferromagnetic. Fig. S31 illustrates the principle magnetic axes of Dy^{III} ions in **1–2UV**, where the angles between the magnetic axes and the vectors connecting the two Dy^{III} ions in **1**, **1UV**, **2** and **2UV** are 2.3°, 2.0°, 2.9° and 2.6°, respectively. These magnetic axes are parallel to each other and closely aligned with the direction connecting the two Dy^{III} ions. This results in an extremely weak transversal component of the induced dipolar field between dysprosium ions, thus significantly reducing the efficiency of the quantum tunnelling mechanism, a process typically highly active in high concentration lanthanide-based SMMs.

Conclusions

We report two compounds $[Dy_2(SCN)_4(L)_2(depma)_2(DEPP)_2]$ (**1**) and $[Dy_2(SCN)_4(L^{Me})_2(depma)_2(DEPP)_2]$ (**2**). Both can undergo a SC–SC photocycloaddition reaction under UV irradiation, to form chain compounds $[Dy_2(SCN)_4L_2(depma_2)(DEPP)_2]_n$ (**1UV**) and $[Dy_2(SCN)_4(L^{Me})_2(depma_2)(DEPP)_2]_n$ (**2UV**). This structural transformation leads to significant alterations in the PL properties and magnetic dynamics of compound **1**. But for compound **2**, the changes in PL and magnetic properties were not pronounced. The introduction of the auxiliary ligand DEPP and the modification of the bridging ligand L result in changes in the stacking pattern of anthracene pair. Consequently, the de-dimerization temperatures of **1UV** (80 °C) and **2UV** (71 °C) are remarkably lower than those of known dianthracene-based compounds, with **2UV** showing the lowest de-dimerization temperatures. We found that the stability of *in situ* formed dianthracene depends largely on the plane-to-plane distance and slip angle of the anthracene pair in the original complex, with the former appearing to be more important. We also investigated the temperature effect on the photocycloaddition reaction of **1** using fluorescence spectroscopy. The reaction kinetics followed the first-order reaction characteristics, with the rate increasing with temperature and peaking at 100 °C. Interestingly, the photocycloaddition reaction of anthracene may still occur even at temperatures reaching complete de-dimerization. This finding enables temperature-controlled regulation of photodimerization/de-dimerization reactions of anthracene, offering potential applications in molecular photonics and devices. In addition, we observed that compounds with their photodimerized products showing lower de-dimerization temperatures may undergo less structural alterations before and after illumination, resulting in smaller changes in luminescence and magnetic properties. Therefore, how to achieve rapid and reversible photodimerization/de-dimerization reactions at relatively low temperatures while eliciting significant luminescence and/or magnetic changes remains a critical challenge for lanthanide anthracene-based materials.

Experimental

Materials and methods

Materials and physical measurements. The ligands 9-diethylphosphonomethylanthracene (depma) were synthesized according to the literature.[81] All other starting reagents and solvents were obtained from commercial sources and used directly. The elemental analysis for C, H and N was performed using a PE 240C analyzer. The infrared (IR) spectra were measured in the range 4000–400 cm^{-1} using KBr pellets on Bruker Tensor 27 spectrometer. The thermogravimetric (TG) analyses were carried out on a Mettler Toledo TGA/DSC instrument in the range of 30–600 °C under N_2 atmosphere with a heating rate of 5 °C min^{-1}. Powder X-ray diffraction (PXRD) data were recorded on a Bruker D8 advance diffractometer with Cu-Kα radiation in a range of 5–50° at room temperature. The differential scanning calorimetry (DSC) measurement was conducted on a Mettler DSC823e instrument at a heating rate of 5 K min^{-1}. The UV/Vis spectra were measured on a PerkinElmer Lambda 950 UV/VIS/NIR spectrometer using powder samples. The steady fluorescence spectra were recorded using Spectrofluorimeter PE LS55. Time resolved fluorescence and quantum yield measurements were performed on an Edinburgh FLS 980 at room temperature. Single crystal fluorescence tests at different temperatures were performed on a home-built widefield microscope with 375-nm CW diode laser as the light source. The PL was collected by an oil immersion objective lens (Olympus UPlanFLN 60×, NA = 1.25) and imaged by an EMCCD camera (iXon Ultra 888, Andor), after passing through a 400-nm longpass filter (ET400LP, Chroma). The ^1H NMR spectra were recorded on BRUKER AVANCE III 400 MHz spectrometer. The dc and ac magnetic susceptibility data were collected on polycrystalline samples by Quantum Design vibrating sample magnetometer (VSM). A drop of Paraffin less than 2 mg was added to avoid the movement and reorientation of samples during measurement. The dc susceptibilities were corrected for diamagnetic contributions of holder, paraffin and sample.[82]

Single crystal X-ray crystallography

Single crystals were used for data collections on Bruker APEX duo diffractometers using graphite-monochromated Mo-Kα radiation (λ = 0.71073 Å). The data were integrated using the Siemens SAINT program.[83] Multiscan absorption corrections

were applied. The structures were solved by intrinsic phasing methods and refined on F^2 by full-matrix least squares using SHELXTL.[84] All the non-hydrogen atoms were refined anisotropically. All H atoms were placed in theoretical positions and refined isotropically. The residual electron densities were of no chemical significance.

Synthesis of $[Dy_2(SCN)_4(L)_2(depma)_2(DEPP)_2]$ (1). To 5 mL of MeCN, 2,6-dimethoxyphenol (HL, 13.4 mg, 0.1 mmol) and Et_3N (14 μL, 0.1 mmol) were sequentially added, followed by 1 mL of the 0.1 mol L^{-1} $Dy(SCN)_3$ solution.[24] The mixture was stirred at room temperature for 5 min. Depma (30.0 mg, 0.1 mmol) and DEPP (15.2 mg, 0.1 mmol) were then added. After 5 min of stirring, the reaction mixture was filtered to afford a clear yellow solution. Slow evaporation of the filtrate at ambient temperature over 24 h afforded yellow block crystals of compound **1**. Yield: 42.9 mg (45.6% based on Dy). Elemental Anal. Calcd (%): C, 45.98; H, 5.04; N, 2.98. Found (%): C, 45.39; H, 5.11; N, 3.07.

Synthesis of $[Dy_2(SCN)_4(L^{Me})_2(depma)_2(DEPP)_2]$ (2). Compound **2** was synthesized using a method similar to that of compound **1**, except that the ligand HL was replaced with 4-methyl-2,6-dimethoxyphenol (HL^{Me}, 16.8 mg, 0.1 mmol). Yield: 41.1 mg (43.1% based on Dy). Elemental Anal. Calcd (%): C, 46.57; H, 5.18; N, 2.94. Found (%): C, 46.14; H, 5.17; N, 3.07.

Author contributions

Y.-H. Q., X.-F. M. and X.-D. H. conducted experiments and analysed the data. Y.-H. Q. and X.-F. M. wrote the manuscript. X. H. and Y. T. performed single crystal fluorescence measurements at different temperatures and the related data analysis. S.-S. B. assisted in the analysis of the single-crystal data. Y.-Q. Z. performed theoretical calculations of magnetic properties and the related data analysis. L.-M. Z. conceived the project and revised the manuscript.

Conflicts of interest

There are no conflicts to declare.

Data availability

CCDC 2455154 (**2**), 2456341 (**1UV**), 2456346 (**2UV**) and 2456349 (**1**) contain the supplementary crystallographic data for this paper.[85a–d]

The data supporting this article have been included as part of the SI. Supplementary information: additional crystallographic details, and other characterizations (PXRD, IR, UV-Vis and photoluminescence spectra, thermal analysis, photographs). See DOI: https://doi.org/10.1039/d5sc04192a.

Acknowledgements

This work was supported by the National Natural Science Foundation of China (22273037, 92356303, 21731003).

References

1 S. J. Loeb, *Chem. Soc. Rev.*, 2007, **36**, 226–235.
2 J. J. Zakrzewski, M. Liberka, J. Wang, S. Chorazy and S. Ohkoshi, *Chem. Rev.*, 2024, **124**, 5930–6050.
3 N. Deorukhkar, C. Egger, L. Guénée, C. Besnard and C. Piguet, *J. Am. Chem. Soc.*, 2024, **146**, 308–318.
4 T. G. Ashebr, H. Li, X. Ying, X.-L. Li, C. Zhao, S. Liu and J. Tang, *ACS Mater. Lett.*, 2022, **4**, 307–319.
5 A. G. Bispo Jr, *Coord. Chem. Rev.*, 2025, **537**, 216685.
6 (*a*) J.-T. Chen, T.-D. Zhou and W.-B. Sun, *Dalton Trans.*, 2023, **52**, 4643–4657; (*b*) P.-Y. Liao, Y. Liu, Z.-Y. Ruan, H.-L. Wang, C.-G. Shi, W. Deng, S.-G. Wu, J.-H. Jia and M.-L. Tong, *Inorg. Chem.*, 2023, **62**, 1075–1085.
7 K. Rogacz, M. Brzozowska, S. Baś, K. Kurpiewska and D. Pinkowicz, *Inorg. Chem.*, 2022, **61**, 16295–16306.
8 X.-J. Luo, Y. Liu, H.-D. Pan, S. Peng, Z.-B. Hu, Q.-H. Teng, Y. Li, F.-P. Liang and K. Wang, *Cryst. Growth Des.*, 2023, **23**, 4825–4835.
9 (*a*) M. Estrader, J. S. Uber, L. A. Barrios, J. Garcia, P. Lloyd-Williams, O. Roubeau, S. J. Teat and G. Aromí, *Angew. Chem., Int. Ed.*, 2017, **56**, 15622–15627; (*b*) J. J. Zakrzewski, R. Jankowski, M. Romanowska, J. Wang, D. Pinkowicz, B. Sieklucka, S.-i. Ohkoshi and S. Chorazy, *Angew. Chem., Int. Ed.*, 2025, **64**, e202424651.
10 Y.-J. Ma, J.-X. Hu, S.-D. Han, J. Pan, J.-H. Li and G.-M. Wang, *J. Am. Chem. Soc.*, 2020, **142**, 2682–2689.
11 X.-Q. Wang, Y.-W. Geng, Z. Wang, C. Xie, T. Han and P. Cheng, *J. Am. Chem. Soc.*, 2025, **147**, 18044–18053.
12 L.-F. Wang, J.-Z. Qiu, Y.-C. Chen, J.-L. Liu, Q.-W. Li, J.-H. Jia and M.-L. Tong, *Inorg. Chem. Front.*, 2017, **4**, 1311–1318.
13 L.-Z. Cai, Q.-S. Chen, C.-J. Zhang, P.-X. Li, M.-S. Wang and G.-C. Guo, *J. Am. Chem. Soc.*, 2015, **137**, 10882–10885.
14 M. Hojorat, H. Al Sabea, L. Norel, K. Bernot, T. Roisnel, F. Gendron, B. L. Guennic, E. Trzop, E. Collet, J. R. Long and S. Rigaut, *J. Am. Chem. Soc.*, 2020, **142**, 931–936.
15 P. Selvanathan, G. Huang, T. Guizouarn, T. Roisnel, G. Fernandez-Garcia, F. Totti, B. Le Guennic, G. Calvez, K. Bernot, L. Norel and S. Rigaut, *Chem.–Eur. J.*, 2016, **22**, 15222–15226.
16 Y. Xin, J. Wang, M. Zychowicz, J. J. Zakrzewski, K. Nakabayashi, B. Sieklucka, S. Chorazy and S. Ohkoshi, *J. Am. Chem. Soc.*, 2019, **141**, 18211–18220.
17 J. Wang, J. J. Zakrzewski, M. Zychowicz, V. Vieru, L. F. Chibotaru, K. Nakabayashi, S. Chorazy and S. Ohkoshi, *Chem. Sci.*, 2021, **12**, 730–741.
18 P. Giri, A. Panda and M. K. Panda, *Chem.–Eur. J.*, 2024, **30**, e202303836.
19 S. Bai, L.-F. Wang, Z.-W. Wu, T. Feng and Y.-F. Han, *Dalton Trans.*, 2022, **51**, 8743–8748.
20 N. Huang, X. Ding, J. Kim, H. Ihee and D. Jiang, *Angew. Chem., Int. Ed.*, 2015, **54**, 8704–8707.
21 M. Servalli, N. Trapp and A. D. Schlüter, *Chem.–Eur. J.*, 2018, **24**, 15003–15012.
22 K. Yuhara and K. Tanaka, *Angew. Chem., Int. Ed.*, 2024, **63**, e202319712.

23 X.-D. Huang, Y. Xu, K. Fan, S.-S. Bao, M. Kurmoo and L.-M. Zheng, *Angew. Chem., Int. Ed.*, 2018, **57**, 8577–8581.
24 X.-D. Huang, G.-H. Wen, S.-S. Bao, J.-G. Jia and L.-M. Zheng, *Chem. Sci.*, 2021, **12**, 929–937.
25 X.-D. Huang, X. Ma and L.-M. Zheng, *Angew. Chem., Int. Ed.*, 2023, **62**, e202300088.
26 Y.-H. Wang, Z.-N. Gao, S. Liang, J. Li, W.-J. Wei, S.-D. Han, Y.-Q. Zhang, J.-X. Hu and G.-M. Wang, *Research*, 2024, **7**, 0411.
27 J.-C. Liu, X.-D. Huang, Q. Zou, S.-S. Bao, X.-Z. Wang, J.-Y. Ma and L.-M. Zheng, *J. Mater. Chem. C*, 2020, **8**, 7369–7377.
28 Q. Zou, T. Shang, X.-D. Huang, Q.-Q. Guo, J.-G. Jia, S.-S. Bao, Y.-Q. Zhang and L.-M. Zheng, *J. Mater. Chem. C*, 2021, **9**, 10749–10758.
29 Q. Zou, J.-C. Liu, X.-D. Huang, S.-S. Bao and L.-M. Zheng, *Chin. Chem. Lett.*, 2021, **32**, 1519–1522.
30 X.-D. Huang, B.-K. Hong, G.-H. Wen, S.-H. Li and L.-M. Zheng, *Chem. Sci.*, 2023, **14**, 1852–1860.
31 Q.-Q. Su, S.-S. Bao, X.-D. Huang, Q. Teng, X.-F. Ma, Y.-H. Qin and L.-M. Zheng, *Cryst. Growth Des.*, 2024, **24**, 10314–10325.
32 X.-F. Ma, X.-D. Huang and L.-M. Zheng, *Cryst. Growth Des.*, 2023, **23**, 1095–1103.
33 X.-D. Huang, X.-F. Ma, T. Shang, Y.-Q. Zhang and L.-M. Zheng, *Inorg. Chem.*, 2023, **62**, 1864–1874.
34 L. Zhu, A. Agarwal, J. Lai, R. O. Al-Kaysi, F. S. Tham, T. Ghaddar, L. Mueller and C. J. Bardeen, *J. Mater. Chem.*, 2011, **21**, 6258.
35 X.-D. Huang, J.-G. Jia, M. Kurmoo, S.-S. Bao and L.-M. Zheng, *Dalton Trans.*, 2019, **48**, 13769–13779.
36 T.-D. Nguyen, M.-T. Lau, K.-L. Hoang, T.-H. Dinh, H.-H. Nguyen and M.-H. Nguyen, *Inorg. Chim. Acta*, 2022, **541**, 121066.
37 D. Casanova, M. Llunell, P. Alemany and S. Alvarez, *Chem.–Eur. J.*, 2005, **11**, 1479–1494.
38 G. M. J. Schmidt, *Pure Appl. Chem.*, 1971, **27**, 647–678.
39 W. T. Carnall, P. R. Fields and K. Rajnak, *J. Chem. Phys.*, 1968, **49**, 4424–4442.
40 X.-F. Ma, Y. Guo, X.-D. Huang, G.-H. Wen, S.-S. Bao, Y.-Q. Zhang and L.-M. Zheng, *Dalton Trans.*, 2022, **51**, 12026–12030.
41 Y. Shen, H. Liu, J. Cao, S. Zhang, W. Li and B. Yang, *Phys. Chem. Chem. Phys.*, 2019, **21**, 14511–14515.
42 S. Wang, H. Liu, S. Zhao, Q. Wu, Z. Yang, D. Yang, Y. Lv, Q. Su, S.-T. Zhang and B. Yang, *Chem. Sci.*, 2025, **16**, 3275–3284.
43 L.-Y. Hsu, S. Maity, Y. Matsunaga, Y.-F. Hsu, Y.-H. Liu, S.-M. Peng, T. Shinmyozu and J.-S. Yang, *Chem. Sci.*, 2018, **9**, 8990–9001.
44 M. Tu, H. Reinsch, S. Rodríguez-Hermida, R. Verbeke, T. Stassin, W. Egger, M. Dickmann, B. Dieu, J. Hofkens, I. F. J. Vankelecom, N. Stock and R. Ameloot, *Angew. Chem., Int. Ed.*, 2019, **58**, 2423–2427.
45 (*a*) R. Gao, Q. Zou, Q.-Q. Su, X.-F. Ma, Y.-H. Qin, R. Liao, S.-S. Bao and L.-M. Zheng, *Chin. Chem. Lett.*, 2025, **36**, 110404; (*b*) R. Gao, S.-S. Bao, Q.-Q. Su, X.-F. Ma and L.-M. Zheng, *Inorg. Chem.*, 2025, **64**, 9303–9313.
46 N. Kariaka, D. Panasiuk, V. Trush, S. Smola, N. Rusakova, V. Dyakonenko, S. Shishkina, A. Lipa, A. Bienko, J. Nasalska, P. Gawryszewska and V. Amirkhanov, *Molecules*, 2025, **30**, 1245.
47 L. Wu, X.-D. Huang, W. Li, X. Cao, W.-H. Fang, L.-M. Zheng, M. Dolg and X. Chen, *JACS Au*, 2024, **4**, 3606–3618.
48 Z. Chernia and D. Gill, *Chem. Phys. Lett.*, 1993, **212**, 57–63.
49 A. Kislyak, H. Frisch, M. Gernhardt, P. H. M. Van Steenberge, D. R. D'hooge and C. Barner-Kowollik, *Chem.–Eur. J.*, 2020, **26**, 478–484.
50 T. J. Gately, W. Sontising, C. J. Easley, I. Islam, R. O. Al-Kaysi, G. J. O. Beran and C. J. Bardeen, *CrystEngComm*, 2021, **23**, 5931–5943.
51 A. Das, A. Danao, S. Banerjee, A. M. Raj, G. Sharma, R. Prabhakar, V. Srinivasan, V. Ramamurthy and P. Sen, *J. Am. Chem. Soc.*, 2021, **143**, 2025–2036.
52 R. Moré, M. Scholz, G. Busse, L. Busse, C. Paulmann, M. Tolkiehn and S. Techert, *Phys. Chem. Chem. Phys.*, 2012, **14**, 10187.
53 W. Li, T. J. Gately, D. Kitagawa, R. O. Al-Kaysi and C. J. Bardeen, *J. Am. Chem. Soc.*, 2024, **146**, 32757–32765.
54 H. Bouas-Laurent, A. Castellan, J.-P. Desvergne and R. Lapouyade, *Chem. Soc. Rev.*, 2000, **29**, 43–55.
55 J. Gemen, M. J. Białek, M. Kazes, L. J. W. Shimon, M. Feller, S. N. Semenov, Y. Diskin-Posner, D. Oron and R. Klajn, *Chem*, 2022, **8**, 2362–2379.
56 S. Kataoka, D. Kitagawa, H. Sotome, S. Ito, H. Miyasaka, C. J. Bardeen and S. Kobatake, *Chem. Sci.*, 2024, **15**, 13421–13428.
57 A. Kislyak, D. Kodura, H. Frisch, F. Feist, P. H. M. Van Steenberge, C. Barner-Kowollik and D. R. D'hooge, *Chem. Eng. J.*, 2020, **402**, 126259.
58 X.-F. Ma, X.-L. Hou, Y.-H. Qin, Q. Teng, S.-S. Bao, Y.-X. Tian and L.-M. Zheng, *Chem. Sci.*, 2025, **16**, 10340–10348.
59 P. Lin, T. J. Burchell, R. Clérac and M. Murugesu, *Angew. Chem., Int. Ed.*, 2008, **47**, 8848–8851.
60 L. Zhang, J. Jung, P. Zhang, M. Guo, L. Zhao, J. Tang and B. Le Guennic, *Chem.–Eur. J.*, 2016, **22**, 1392–1398.
61 M. Kong, X. Feng, J. Wang, Y.-Q. Zhang and Y. Song, *Dalton Trans.*, 2021, **50**, 568–577.
62 H.-R. Tu, W.-B. Sun, H.-F. Li, P. Chen, Y.-M. Tian, W.-Y. Zhang, Y.-Q. Zhang and P.-F. Yan, *Inorg. Chem. Front.*, 2017, **4**, 499–508.
63 K. S. Cole and R. H. Cole, *J. Chem. Phys.*, 1941, **9**, 341–351.
64 S. Mukherjee, J. Lu, G. Velmurugan, S. Singh, G. Rajaraman, J. Tang and S. K. Ghosh, *Inorg. Chem.*, 2016, **55**, 11283–11298.
65 P. Hu, L. Cao, A. Liu, Y. Zhang, T. Zhang and B. Li, *Dalton Trans.*, 2021, **50**, 12814–12820.
66 W. Zhang, P. Chen, H. Li, Y. Zhang, P. Yan and W. Sun, *Chem.–Asian J.*, 2018, **13**, 1725–1734.
67 Y. Ma, Y. Zhai, Q. Luo, Y. Ding and Y. Zheng, *Angew. Chem., Int. Ed.*, 2022, **61**, e202206022.
68 L. Gu and R. Wu, *Phys. Rev. B*, 2021, **103**, 014401.
69 M. Briganti, F. Santanni, L. Tesi, F. Totti, R. Sessoli and A. Lunghi, *J. Am. Chem. Soc.*, 2021, **143**, 13633–13645.

70 I. F. Galván, M. Vacher, A. Alavi, C. Angeli, F. Aquilante, J. Autschbach, J. J. Bao, S. I. Bokarev, N. A. Bogdanov, R. K. Carlson, L. F. Chibotaru, J. Creutzberg, N. Dattani, M. G. Delcey, S. S. Dong, A. Dreuw, L. Freitag, L. M. Frutos, L. Gagliardi, F. Gendron, A. Giussani, L. González, G. Grell, M. Y. Guo, C. E. Hoyer, M. Johansson, S. Keller, S. Knecht, G. Kovacevic, E. Källman, G. L. Manni, M. Lundberg, Y. J. Ma, S. Mai, J. P. Malhado, P. Å. Malmqvist, P. Marquetand, S. A. Mewes, J. Norell, M. Olivucci, M. Oppel, Q. M. Phung, K. Pierloot, F. Plasser, M. Reiher, A. M. Sand, I. Schapiro, P. Sharma, C. J. Stein, L. K. Sørensen, D. G. Truhlar, M. Ugandi, L. Ungur, A. Valentini, S. Vancoillie, V. Veryazov, O. Weser, T. A. Wesołowski, P.-O. Widmark, S. Wouters, A. Zech, J. P. Zobel and R. Lindh, *J. Chem. Theory Comput.*, 2019, **15**, 925–5964.

71 L. F. Chibotaru, L. Ungur and A. Soncini, *Angew. Chem., Int. Ed.*, 2008, **47**, 4126–4129.

72 L. Ungur, W. Van den Heuvel and L. F. Chibotaru, *New J. Chem.*, 2009, **33**, 1224–1230.

73 L. F. Chibotaru, L. Ungur, C. Aronica, H. Elmoll, G. Pilet and D. Luneau, *J. Am. Chem. Soc.*, 2008, **130**, 12445–12455.

74 A. Lunghi, F. Totti, R. Sessoli and S. Sanvito, *Nat. Commun.*, 2017, **8**, 14620–14626.

75 F. Lu, M. M. Ding, J.-X. Li, B.-L. Wang and Y.-Q. Zhang, *Dalton Trans.*, 2020, **49**, 14576–14583.

76 F. Lu, W.-X. Guo and Y.-Q. Zhang, *Inorg. Chem.*, 2022, **61**, 295–301.

77 M.-M. Ding, T. Shang, R. Hu and Y.-Q. Zhang, *Dalton Trans.*, 2022, **51**, 3295–3303.

78 T. Shang, F. Lu, J. Tao and Y.-Q. Zhang, *J. Phys. Chem. A*, 2023, **127**, 3088–3095.

79 D.-M. Zhu, F. Lu, X.-L. Zhang and Y.-Q. Zhang, *Inorg. Chem.*, 2025, **64**, 4209–4212.

80 M. E. Lines, *J. Chem. Phys.*, 1971, **55**, 2977–2984.

81 D.-K. Cao, Y.-W. Gu, J.-Q. Feng, Z.-S. Cai and M. D. Ward, *Dalton Trans.*, 2013, **42**, 11436–11444.

82 O. Kahn, *Molecular Magnetism*, Wiley-VCH, New York, 1993.

83 SAINT, *Version 8.40A Program for Data Extraction and Reduction*, Bruker Nano. Inc., 2019.

84 SHELXT 2014/5, Sheldrick, 2014; SHELXL 2018/3, Sheldrick. 2018.

85 (*a*) Y.-H. Qin, X.-F. Ma, X. Hou, X.-D. Huang, S.-S. Bao, Y. Tian, Y.-Q. Zhang and L.-M. Zheng, CCDC 2455154: Experimental Crystal Structure Determination, 2025, DOI: **10.5517/ccdc.csd.cc2ndsjd**; (*b*) Y.-H. Qin, X.-F. Ma, X. Hou, X.-D. Huang, S.-S. Bao, Y. Tian, Y.-Q. Zhang and L.-M. Zheng, CCDC 2456341: Experimental Crystal Structure Determination, 2025, DOI: **10.5517/ccdc.csd.cc2ng0tz**; (*c*) Y.-H. Qin, X.-F. Ma, X. Hou, X.-D. Huang, S.-S. Bao, Y. Tian, Y.-Q. Zhang and L.-M. Zheng, CCDC 2456346: Experimental Crystal Structure Determination, 2025, DOI: **10.5517/ccdc.csd.cc2ng0z4**; (*d*) Y.-H. Qin, X.-F. Ma, X. Hou, X.-D. Huang, S.-S. Bao, Y. Tian, Y.-Q. Zhang and L.-M. Zheng, CCDC 2456349: Experimental Crystal Structure Determination, 2025, DOI: **10.5517/ccdc.csd.cc2ng128**.